Geophysical Research Letters

RESEARCH LETTER
10.1029/2019GL082408

Key Points:
- Atmospheric heating preferentially reduces weak precipitation
- A cancellation between thermodynamic and dynamic effects maintains the intensity of strong precipitation
- Free-tropospheric heating warms the boundary layer mainly through reducing rain reevaporation

Supporting Information:
- Supporting Information S1

Correspondence to:
X. R. Chua,
xchua@princeton.edu

Citation:
Chua, X. R., Ming, Y., & Jeevanjee, N. (2019). Investigating the fast response of precipitation intensity and boundary layer temperature to atmospheric heating using a cloud-resolving model. *Geophysical Research Letters*, *46*. https://doi.org/10.1029/2019GL082408

Received 12 FEB 2019
Accepted 15 JUL 2019
Accepted article online 22 JUL 2019

Investigating the Fast Response of Precipitation Intensity and Boundary Layer Temperature to Atmospheric Heating Using a Cloud-Resolving Model

Xin Rong Chua[1], Yi Ming[1,2], and Nadir Jeevanjee[3]

[1]Program in Atmospheric and Oceanic Sciences, Princeton University, Princeton, NJ, USA, [2]Geophysical Fluid Dynamics Laboratory, Princeton, NJ, USA, [3]Department of Geosciences, Princeton University, Princeton, NJ, USA

Abstract Coarse-resolution global climate models cannot explicitly resolve the intensity distribution of tropical precipitation and how it responds to a forcing. We use a cloud-resolving model to study how imposed atmospheric radiative heating (such as that caused by greenhouse gases or absorbing aerosols) may alter precipitation intensity in the setting of radiative-convective equilibrium. It is found that the decrease in total precipitation is realized through preferentially reducing weak events. The intensity of strong precipitation events is maintained by a cancellation between the moistening of air parcels and weakening of updrafts. A boundary layer energy budget analysis suggests that free-tropospheric heating raises boundary layer temperatures mainly through a reduction in rain reevaporation. This insight leads to a predictive scaling for the surface sensible and latent flux changes. The results imply that cloud microphysical processes play a key role in shaping the temperature and precipitation responses to atmospheric heating.

1. Introduction

Greenhouse gases and absorbing aerosols warm the climate by absorbing longwave and shortwave radiation, respectively. Greenhouse gases represent the strongest anthropogenic climate forcing, with top-of-the-atmosphere values of 2.54–3.12 W/m^2 (Myhre et al., 2013). Unlike well-mixed greenhouse gases, unevenly distributed absorbing aerosols can lead to local top-of-the-atmosphere forcing exceeding 20 W/m^2 (e.g., Strong et al., 2015). The radiative heating gives rise to a fast (days to months) atmosphere-land response and a slow (years or longer) response that involves the ocean (e.g., Andrews & Forster, 2010). Given the different time scales, the two responses can be approximated as distinct. In fact, global climate model (GCM) simulations indicate that the fast response to atmospheric absorption acts to reduce global-mean precipitation, while the slow response has the opposite effect (Andrews et al., 2010; Fläschner et al., 2016; Ming et al., 2010). Thus, one can study the fast response in isolation from the slow response.

On fast time scales, an increase in atmospheric radiative heating must be partially balanced by a reduction in surface latent heat flux (and mean precipitation; Andrews et al., 2010; Bala et al., 2010; Dinh & Fueglistaler, 2017; Richardson et al., 2015). This change in mean precipitation need not scale with, or even agree in sign, with those of precipitation extremes. Under a quadrupling of CO_2, GCMs consistently simulate reductions in mean precipitation (−3% to −8%) but disagree on the sign of the change in annual maximum daily precipitation (Sillmann et al., 2017).

Besides the lack of consensus among models identified by Sillmann et al. (2017), there are many well-known reasons to doubt the capability of GCMs in simulating extreme precipitation with parameterized moist convection (O'Gorman, 2015). GCMs typically underestimate intense precipitation when compared with observations, with the biases being more severe for low-resolution GCMs (1° or coarser; Kopparla et al., 2013; O'Brien et al., 2016; Sillmann et al., 2013; Stephens et al., 2010). While the convective parameterization of a GCM can be altered to better match observations, a troubling sign is that such a modification can lead to larger changes in the frequency of heavy rain than a 2 K increase in sea surface temperatures (Wilcox & Donner, 2007), casting in doubt the utility of GCMs in studying extreme precipitation changes.

In light of the limited resolution of GCMs, we turn to cloud-resolving models on a limited-area domain, which can produce realistic simulations of heavy rain events when forced with proper boundary conditions

(e.g., Fan et al., 2015; Hodzic & Duvel, 2018; Lee et al., 2016). Since we aim to investigate the fast response to atmospheric heating, we intentionally move away from detailed simulation of a particular region or event in favor of a setting that is more representative of the climate system as a whole, namely, radiative-convective equilibrium (RCE). RCE is an idealized representation of the atmosphere where radiation and convection balance in the absence of lateral energy transport. One advantage of RCE is that both energy and moisture are conserved within the atmosphere, which need not be the case for individual events. RCE studies of surface warming (e.g., Muller et al., 2011; Romps, 2011) have identified a strong thermodynamic link between precipitation intensity and boundary layer moisture and a dynamic effect from changes in vertical velocity. However, the relative magnitudes of the two effects in the fast response remains unknown.

In this study, we investigate the fast response of precipitation intensity to atmospheric heating in a cloud-resolving model. This motivates us to also analyze the boundary layer energy balance in order to better identify the physical mechanisms through which elevated heating affects boundary layer temperature and humidity. Existing works have focused on the balance among surface sensible heating, radiative cooling, and entrainment of free-tropospheric air into the boundary layer (Ball, 1960; Lilly, 1968). The entrainment term is often parameterized as a fixed fraction of the surface sensible heat flux (0.2 or 0.25 in Betts, 1973; Betts & Ridgway, 1989; Betts, 2000; Cronin, 2013; Tennekes, 1973), implying that the sensible heat flux is tightly coupled to the boundary layer radiative cooling. While Betts (2000) later recognized that reevaporative cooling might contribute to the boundary layer energy balance, a possible change in reevaporation under warming is not taken into account explicitly in the analytical models of climate sensitivity (Cronin, 2013; Takahashi, 2009). To guide future theoretical development, we systematically evaluate the responses of the boundary layer energy budget to boundary layer versus free-tropospheric heating.

2. Methods

We use the Advanced Research Weather Research and Forecasting model configured to run in RCE (Wang & Sobel, 2011). Radiative transfer is reduced to a prescribed cooling rate in the troposphere ($T > 207.5$ K), and Newtonian relaxation in the stratosphere to 200 K on a time scale of 5 days (Pauluis & Garner, 2006). This highly idealized radiation scheme allows us to focus on the effects of imposed atmospheric heating without complicating factors such as water vapor feedback and cloud radiative effect. Subgrid diffusion is parameterized following the YSU boundary layer scheme (Hong et al., 2006) in the vertical direction, and the Smagorinsky two-dimensional scheme in the horizontal. The single-moment Purdue-Lin microphysics scheme (Chen & Sun, 2002; Lin et al., 1983; Rutledge & Hobbs, 1984) contains six species: water vapor, cloud water, cloud ice, rain, snow, and graupel. Surface sensible and latent heat fluxes (*SH* and *LH*, respectively; both in watts per square meter) are calculated using the bulk aerodynamic formula with a constant (0.005 $\mathrm{kg{\cdot}m^{-2}{\cdot}s^{-1}}$) composed of a drag coefficient of 0.001, a near-surface air density of 1 $\mathrm{kg/m^3}$ and a constant near-surface wind speed of 5 m/s:

$$SH = 0.005 c_p (T_s - T_a) \tag{1}$$

$$LH = 0.005 L (q_{\mathrm{sat}} - q_a), \tag{2}$$

where c_p is the specific heat capacity of dry air (1004.5 $\mathrm{J{\cdot}kg^{-1}{\cdot}K^{-1}}$), L the latent heat of vaporization of water in typical atmospheric conditions (2.5×10^6 J/kg), T_s the surface temperature, T_a the lowest model level (or near-surface) temperature, q_{sat} the saturated water vapor mixing ratio at T_s, and q_a the lowest model level water vapor mixing ratio. As T_s and q_{sat} are fixed, it is clear from equations (1) and (2) that the only way to alter *SH* and *LH* is by adjusting near-surface boundary layer temperature and humidity (T_a and q_a).

All simulations are performed on a doubly periodic domain of 96×96 grid points with a horizontal spacing of 2 km. There are 50 vertical levels, nine of which are in the lowest 1 km. Domain-averaged winds are relaxed to zero on a time scale of 2 hr to prevent wind shear from developing, similar to Tompkins and Semie (2017). The surface temperature is set to 301.15 K, making the lower boundary conditions horizontally homogenous. The two control simulations with different microphysical assumptions (to be discussed) are initialized with a warm bubble and are first performed for 240 model days; the perturbation simulations are branched off day 180 of their respective controls and last 60 model days. The last 20 days of hourly-mean outputs from each simulation are analyzed. We use five consecutive, nonoverlapping 20-day periods from extensions of the control simulations (days 220–320) for assessing the noise level of any given variable. The difference between a control and a perturbation is considered significant if it rises above the noise level.

Table 1
Domain-Averaged Tropospheric Radiative Cooling (RA, W/m^2), Surface Sensible Heat Flux (SH, W/m^2), Surface Latent Heat Flux (LH, W/m^2), Near-Surface Temperature (T_a, K), Near-Surface Water Vapor Mixing Ratio (q_a, g/kg), Precipitation (P, mm/day), and Changes in the Perturbation Cases

Experiment	*RA*	*SH*	*LH*	T_a	q_a	*P*
BASE	−145	19.5	127	297.3	14.4	4.4
δHEAT	72	−14.7	−54.9	2.9	4.3	−1.9
δA850	59	−11.1	−45.8	2.2	3.5	−1.6
δB850	13	−4.2	−7.5	0.8	0.6	−0.3
BASE*	−145	9.4	137	299.3	13.6	4.7
δHEAT*	72	−9.3	−61.1	1.9	4.8	−2.1
δA850*	59	−4.7	−53.3	0.9	4.1	−1.8
δB850*	13	−6.3	−5.6	1.3	0.5	−0.2

Note. All changes are significant.

The prescribed radiative cooling rate is at the default value (−1.5 K/day) in the first control simulation (BASE). It is reduced by half to −0.75 K/day throughout the troposphere in HEAT. To isolate the boundary layer response to free-tropospheric heating, we separate the uniform radiative heating into two complementary differential heating cases: halving the cooling only above 850 hPa (A850) and below (B850). To assess the importance of rain reevaporation in communicating free-tropospheric heating to the boundary layer, we repeat all the simulations with a model configuration in which the rate of rain reevaporation in the cloud microphysics scheme is reduced by an factor of 10. The four additional cases are denoted by adding an asterisk to the original case names. We will refer to the two groups of experiments as full and partial reevaporation, respectively. Throughout this paper, a response to heating is denoted with a δ.

3. Results

3.1. Domain-Averaged Responses

Through the energetic constraint, the radiative heating alters surface fluxes, thereby affecting temperature, moisture, and precipitation. We begin by examining a set of key domain-averaged quantities and their changes resulting from forced heating (Table 1). Relative to BASE, the tropospheric radiative cooling (from the surface to 200 hPa) is cut by half in HEAT. The resulting net heating is balanced by reducing both surface sensible and latent heat fluxes with a ratio of δSH to δLH at 0.27, which differs significantly from the Bowen ratio in BASE (0.15), suggesting that radiative cooling plays a role in determining the Bowen ratio. Consistent with equations (1) and (2), the near-surface temperature (T_a) increases by 2.9 K, while the near-surface water vapor mixing ratio (q_a) increases by 30%. The increase in q_a in HEAT occurs alongside a 8.5% (relative) increase in near-surface relative humidity (Text S1 in the supporting information). More quantitatively, according to equations (1) and (2), the changes in *SH* (δSH) and *LH* (δLH) are proportional to δT_a and δq_a, respectively, meaning that one can tie the near-surface temperature and humidity changes directly to the imposed heating. It is, nonetheless, unclear what determines the relative contributions of surface sensible and latent heating, a point to which we will return in section 4. The domain-averaged precipitation (equivalent to latent heat flux) reduces by 43%, which is less than the relative decrease in radiative cooling.

For the two differential heating cases, the column-integrated change in radiative cooling in A850 is about 4.5 times of that in B850. This is understandable as it is approximately proportional to the pressure depth to which the perturbations are applied (i.e., $[850-200]/[1,000-850]$). The ratio is 2.8 for δT_a, and 5.8 for δq_a and δP, suggesting that elevated heating is less effective at modifying surface sensible flux (near-surface temperature), but more so at altering surface latent heat flux (near-surface precipitation and moisture). Somewhat surprisingly, the free-tropospheric heating has a substantial warming effect on the near surface, especially given that most of the sensible heating from the YSU scheme is placed in the boundary layer. This suggests that when conjecturing a quantitative theory for the partitioning of surface sensible and latent heating, one has to take into account the vertical distribution of atmospheric radiative heating and an energetic coupling between the free troposphere and boundary layer (to be investigated in section 3.3).

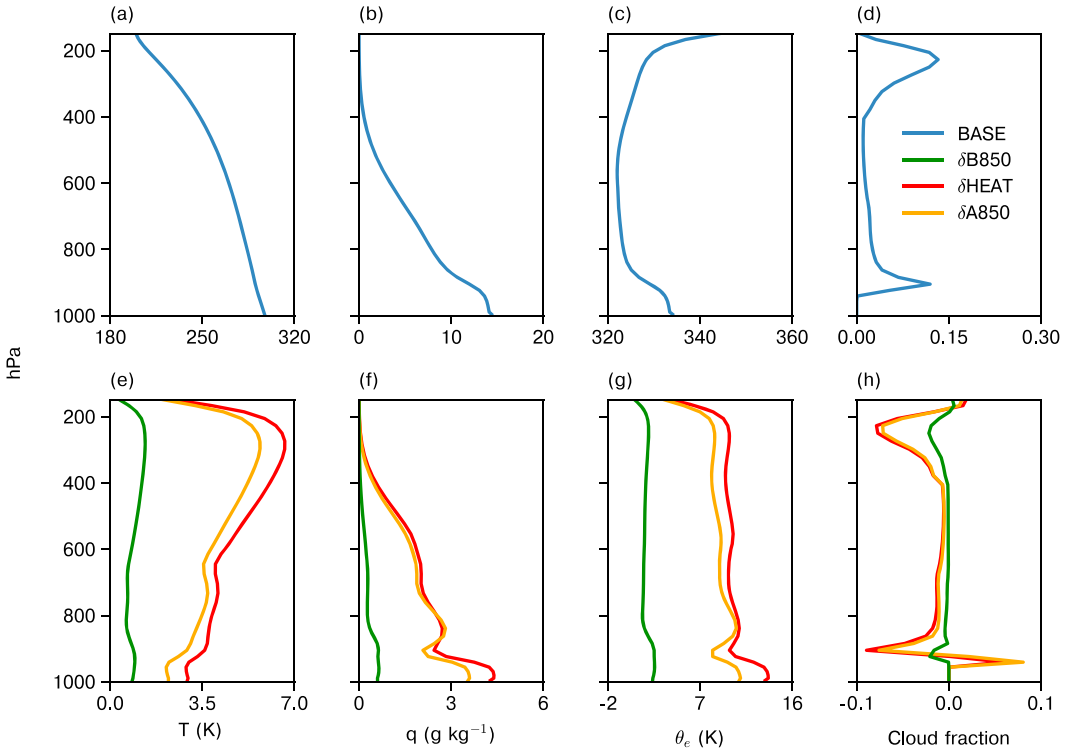

Figure 1. Vertical profiles of (a) temperature (T, K), (b) water vapor mixing ratio (q, g/kg), (c) equivalent potential temperature (θ_e, K), and (d) cloud fraction in BASE. (e–h) Changes in (a)–(d) due to heating (prefixed by δ) in HEAT, A850, and B850. All changes rise significantly above the noise level.

Relative to BASE, the decreased microphysical cooling in BASE* warms the boundary layer by 2 K, reducing the surface sensible heat flux (*SH*). The tropospheric energy balance is restored by increasing the surface latent heat flux, which is consistent with lower near-surface humidity. The response of *SH* to the heating in HEAT* is much smaller (−9.3 W/m^2) than that of HEAT (−14.7 W/m^2). Note that *SH* is close to zero in HEAT*. As compared to the full reevaporation counterparts, elevated heating becomes less effective in inducing near-surface warming under partial reevaporation (1.9 K in HEAT* versus 2.9 K in HEAT, and 0.9 in A850* versus 2.2 K in A850). Consequently, the reduction in latent heat (precipitation) is more pronounced in the partial reevaporation cases with free-tropospheric heating.

The radiative heating also alters the vertical profiles of key atmospheric quantities. Figure 1 shows the vertical profiles of temperature (T), water vapor mixing ratio (q), equivalent potential temperature (θ_e), and cloud fraction in BASE (top row) and their changes in the perturbation cases (bottom row). The temperature structure in RCE follows that of a moist adiabat (Figure 1a), and to first-order sets the vertical structure of water vapor (Figure 1b) in the free troposphere. The θ_e shows a first baroclinic mode structure (Figure 1c), with a minimum at around 500 hPa. Under heating, the near-surface warming extends throughout the troposphere, with appreciable amplification in the middle and upper troposphere, as a consequence of moist adiabatic control (Figure 1e). In contrast, the accompanying increase in q is bottom heavy, as in the control (Figure 1f). The θ_e increases rather uniformly throughout the troposphere (Figure 1g). As in Wang and Sobel (2011), a grid is defined as cloudy if the total cloud condensate (water and ice) exceeds 0.005 g/kg. Cloud fraction has two maxima in the vertical direction (Figure 1d). One can regard the lower one approximately as the lifting condensation level. It becomes lower in HEAT as the near-surface relative humidity increases (Romps, 2017). Note that the lifting condensation level remains above 965 hPa (the boundary layer top used in this paper) in all experiments. The cloud fraction in HEAT is approximately half of that in BASE (Figures 1d and 1h). The domain-mean responses are qualitatively similar in the other simulations (e.g., Figure S2). Next, we examine connections between domain-mean quantities and precipitation intensity.

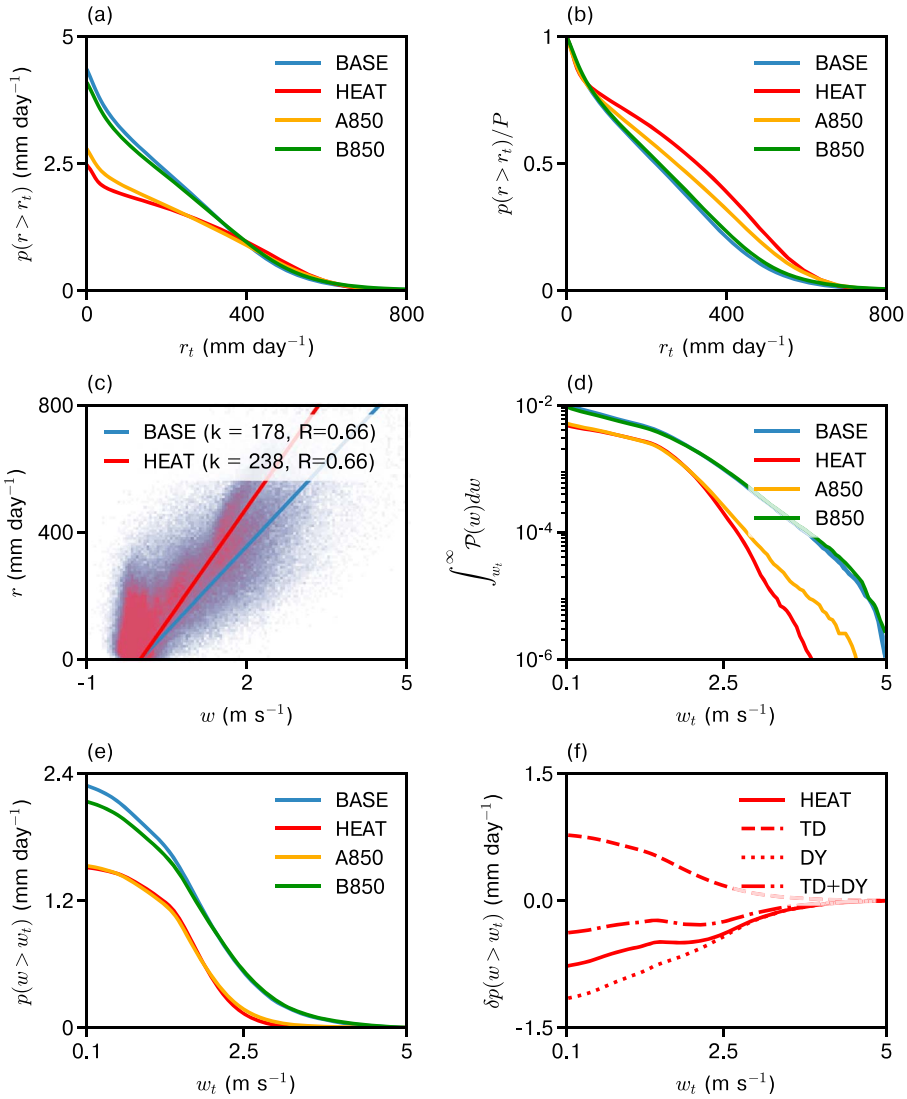

Figure 2. (a) The domain-averaged precipitation ($p[r > r_t]$, mm/day) of the events whose hourly precipitation rates exceed r_t (mm/day) in the full reevaporation experiments. (b) $p(r > r_t)$ normalized by domain-mean precipitation P. (c) The scatter plot of r (mm/day) against 500-hPa vertical velocity (w, m/s) for BASE and HEAT. The solid lines are the best fit lines with zero intercept for $w > 0.1$ m/s. (d) The probability of w exceeding a threshold w_t (m/s), or $\int_{w_t}^{\infty} \mathcal{P}(w)dw$, for $w_t > 0.1$ m/s. (e) The domain-averaged precipitation ($p(w > w_t)$, mm/day) of the events where w exceeds w_t, estimated with equation (3). (f) The difference in $p(w > w_t)$ (mm/day) between BASE and HEAT, and its thermodynamic and dynamic components and their sum, estimated with equation (4).

3.2. Precipitation Intensity

Here, we explore whether the reduction in domain-mean precipitation shifts the intensity distribution of precipitation. The domain-averaged precipitation of the events at grid points where the hourly precipitation rate r exceeds a threshold value r_t (in mm/day) is denoted as $p(r > r_t)$ (Figure 2a). By definition, $p(r > 0)$ is the domain-averaged precipitation of all events (P), which was discussed in section 3.1. Figure 2b shows $p(r > r_t)$ normalized by the domain-mean precipitation P. In BASE, the top 50% of precipitation have precipitation rates exceeding 210 mm/day. Despite the substantial (43%) reduction in HEAT, the top 50% of precipitation falls with precipitation rates exceeding 320 mm/day in HEAT. In this sense, the reduction in precipitation is realized through a reduction in weak, rather than strong, events.

Figure 2c plots the hourly precipitation rate against 500-hPa (nearest model level) vertical velocity (w) for all grid points in BASE and HEAT. Both quantities are strongly correlated, especially for the events with appreciable positive (upward) w (greater than ~ 0.1 m/s); a linear regression through the origin yields $R =$

0.66 for BASE and HEAT. Yet, the slope (k) for HEAT is 34% larger than for BASE, meaning that the same ascending motion generates considerably more precipitation in the former. This is consistent with the 30% increase in the average near-surface water vapor mixing ratio (q_a) as discussed above. One may also gather that vertical velocity is generally weaker in HEAT than in BASE.

Figure 2d shows the probability of w exceeding a threshold w_t for $w_t > 0.1$ m/s, or $\int_{w_t}^{\infty} \mathcal{P}(w)dw$, where $\mathcal{P}(w)$ is the probability density function of w. Ascents are relatively rare; in BASE, only 1.0% of the grids have w larger than 0.1 m/s. The probability decreases by more than 3 orders of magnitude as w_t increases to 5 m/s. In HEAT, ascending motions become even less likely across the entire range of w_t, affirming the impression of weaker ascents from Figure 2c. The idealized calculations of Pendergrass and Gerber (2016) suggests that a shift toward strong events is accompanied by increased skewness in $\mathcal{P}(w)$. Indeed, skewness increases by 22% in HEAT (not shown).

To better understand the different responses of strong versus weak events, we write the domain-averaged precipitation of the events with w greater than a certain positive value w_t [$p(w > w_t)$, w_t; m/s] approximately as follows:

$$p(w > w_t) \approx k \int_{w_t}^{\infty} w\mathcal{P}(w)\mathrm{d}w. \tag{3}$$

$p(w > 0.1)$ is 2.3 mm/day in BASE, which accounts for slightly more than half of the total precipitation (Figure 2e). The remaining is associated with very weak ascents (less than 0.1 m/s) and descents. $p(w > w_t)$ is consistently smaller in HEAT for w_t greater than 0.1 m/s, making it easier to interpret the difference between the two cases than in terms of $p(r)$ (Figure 2a). By assuming that k is independent of $\mathcal{P}(w)$, one can linearly decompose the difference ($\delta p[w > w_t]$) into the thermodynamic (δk) and dynamic ($\delta\mathcal{P}$) terms:

$$\delta p(w > w_t) \approx \delta k \int_{w_t}^{\infty} w\mathcal{P}(w)\mathrm{d}w + k \int_{w_t}^{\infty} w\delta\mathcal{P}(w)\mathrm{d}w. \tag{4}$$

Figure 2f indicates that although neglecting the nonlinearities underestimates the difference between BASE and HEAT, it does capture some important characteristics of the simulations (e.g., $\delta p[w > w_t]$ generally decreases as w_t increases). While the thermodynamic effect owing to higher near-surface water vapor mixing ratio acts to enhance precipitation, the dynamic effect in the form of weaker ascents tends to lower precipitation. As the dynamic effect outweighs the thermodynamic effect, the net result is a reduction of precipitation at a given w_t. A similar cancellation is seen when the full vertical velocity distribution is included (e.g., Fildier et al., 2017; O'Gorman & Schneider, 2009; not shown). Additional experiments with doubling domain size, increasing sea surface temperatures (+10 K) and halving the amount of prescribed heating confirm the shift toward strong precipitation and the compensation between thermodynamic and dynamic effects (Figure S3), and illustrate that the sign of the change in extreme (99.99th percentile) precipitation depends on the configuration used (Table S1). The cancellation between the thermodynamic and dynamic effects for strong events implies that energy balance is maintained by preferentially reducing weak events. The key role of boundary layer moisture in maintaining the intensity of strong precipitation events motivates an analysis of the surface sensible versus the latent heat response.

3.3. Boundary Layer Energy Balance

In equilibrium, the processes that influence surface sensible heat flux (SH) are encapsulated in the boundary layer energy balance: $SH + RA_b + RE + EX = 0$. SH is the main energy source for the boundary layer in BASE (Figure 3a). Additional heating is realized through the exchange of sensible heat with the free troposphere, either explicitly resolved or parameterized at the sub–grid scale (EX), which is inferred as a residual. The sink terms are radiative cooling (RA_b) and reevaporative cooling (RE), calculated by integrating the radiative and microphysical heating rates over the boundary layer. The latter takes place as rain falls through the unsaturated boundary layer and is thus microphysical in nature. Somewhat surprisingly, the magnitude of reevaporative cooling is larger than that of radiative cooling, which is often presumed to be the dominant sink term.

Figure 3b summarizes how the individual terms vary in the perturbation cases. Although imposed radiative heating is clearly present in HEAT, the main balance is between SH and RE, both of which decrease substantially in magnitude. As A850 and B850 add up roughly to HEAT, one can see that the boundary layer radiative heating is balanced almost entirely by lowering SH, as is the case in B850. The large reduction in

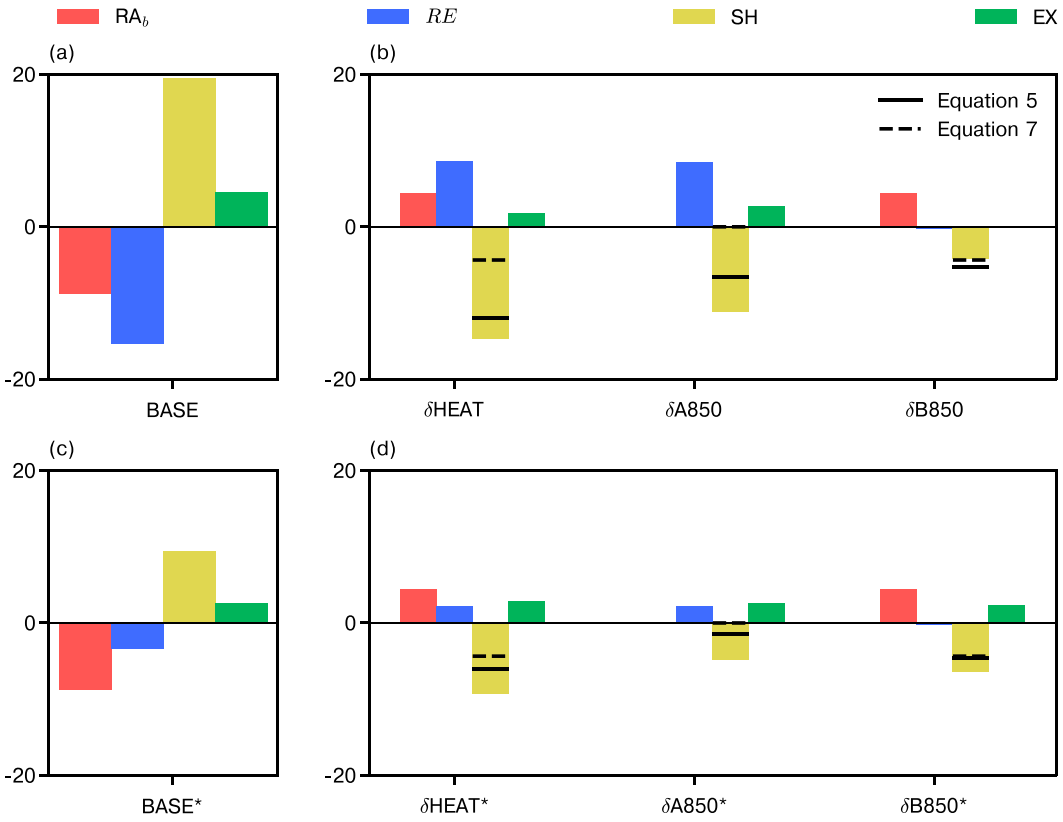

Figure 3. (a) The individual terms in the boundary layer energy balance (W/m^2) in BASE: surface sensible heating (*SH*), radiative cooling (RA_b), reevaporative cooling (*RE*), and the exchange of sensible heat with the free troposphere (*EX*). (b) Changes in HEAT, A850, and B850. (c, d) Same as (a) and (b) but for the partial reevaporation cases. The solid and dashed lines denote the change in *SH* calculated from equations (5) and (7), respectively.

RE seen in HEAT can be attributed to the radiative heating above 850 hPa, and amounts to a warming effect on the boundary layer. This is consistent with lower *SH* and higher near-surface temperature (Table 1). The changes in *EX* are small compared to those in *SH*.

One can define precipitation efficiency (ϵ) as the ratio of precipitation (P) over column-integrated condensation (C; Zhao, 2014), with a value of 0.33 in BASE. Column-integrated reevaporation (E), which is equal to the difference between C and P (i.e., $C - P$) can be written as $P(1 - \epsilon)/\epsilon$. As ϵ is little changed across the cases, the fractional changes in column-integrated reevaporation and precipitation are similar (Figure S4). The scaling of Lutsko and Cronin (2018) works reasonably well for the fraction of precipitation that is reevaporated, but should not be confused with a general scaling for reevaporation (Text S2).

The partial reevaporation simulations allow us to further assess the importance of reevaporation. Despite having the same boundary layer radiative cooling as BASE, the magnitudes of the surface sensible heating and the exchange term are much reduced in BASE*, presumably due to the suppressed reevaporative cooling (Figure 3c). The response to free-tropospheric heating is also muted considerably in A850*; the resulting reduction in *SH* is less than half of that in A850. The same is true for near-surface temperature T_a (Table 1). This reaffirms the importance of reevaporative cooling in communicating the effect of free-tropospheric heating to the boundary layer and surface fluxes. In summary, heating the free-troposphere reduces mean precipitation and rain reevaporation, leading to boundary layer warming.

4. Discussion and Summary

The results show that the vertical distribution of radiative heating is key to determining the relative roles of surface sensible and latent heat adjustments in reestablishing the tropospheric energy balance. In particular, reevaporative cooling is the main process through which the effect of free-tropospheric heating can be

felt by the boundary layer. Thus, reevaporation has to be considered explicitly in any attempt to develop a quantitative theory of the surface sensible heat flux response to atmospheric heating.

If one assumes that the free-tropospheric energy balance can be approximated as radiative cooling balancing out latent heating, it follows that the fractional change of precipitation is equal to that of the free-tropospheric radiative cooling ($\delta P/P = \delta RA_f/RA_f$). As discussed in section 3.3, the fractional changes of the boundary layer reevaporative cooling is approximately equal to that of precipitation. Thus, δRE can be written as $\alpha\delta RA_f$, where α is the ratio of RE to RA_f in the control case. If the exchange term does not vary appreciably with imposed heating, the boundary layer energy balance leads to the following expression of the surface sensible heat flux change:

$$\delta SH = -\delta RA_b - \alpha\delta RA_f. \tag{5}$$

Furthermore, its latent heat counterpart can be derived from the tropospheric energy balance:

$$\delta LH = (\alpha - 1)\delta RA_f. \tag{6}$$

This constitutes a predictive scaling of δSH and δLH in response to δRA_b and δRA_f as α (0.11 in BASE) depends only on values in the control experiment. The predicted δSH (solid lines in Figure 3) is in good agreement with the simulations (bars). According to this theory, free-tropospheric heating reduces LH more than SH as long as α is smaller than 0.5. Also, boundary layer heating decreases SH only.

The approximation used in Takahashi (2009) and Cronin (2013) can be viewed as a special case of equation (5) with $\alpha = 0$:

$$\delta SH = -\delta RA_b. \tag{7}$$

The partial reevaporation experiments allow us to test the theory for a small value of α (0.02 in BASE*) that approaches this special case. Indeed, the predictions from equations (5) and (7) are much closer in the partial reevaporation than the full reevaporation experiments. In other words, the $\alpha\delta RA_f$ term in equation (5) greatly improves the accuracy of the predicted δSH by incorporating the effect of reevaporation in coupling the boundary layer and the free troposphere. To generalize our results to the full climate response, one must account for changes in precipitation efficiency under surface warming (Lutsko & Cronin, 2018) and possible changes in the large-scale circulation (e.g., Lutsko & Cronin, 2018; Wing & Cronin, 2016)

In summary, imposed radiative heating reduces domain-averaged precipitation (evaporation) by increasing boundary layer water vapor, a thermodynamic effect that tends to enhance precipitation rate at a given vertical velocity. This effect opposes the weakening of ascents (a dynamic effect) and serves to maintain the precipitation from strong events. The decrease in domain-averaged precipitation is realized mainly through weak events. A key finding is that free-tropospheric radiative heating affects the boundary layer primarily by weakening the reevaporative cooling. This insight leads to a predictive scaling of the surface latent and sensible heat flux changes caused by radiative heating.

Acknowledgments
Shuguang Wang provided the source code for the modified version of WRF and valuable advice. Data and scripts used in this paper are available at ftp://data1.gfdl.noaa.gov/users/Xin.Rong.Chua/WRF_heat/WRF website. The analysis was aided by the "aospy" package. X. R. C. acknowledges funding from the National Research Foundation of Singapore and the Cooperative Institute for Climate Science and wishes to thank Hailey Shin, Usama Anber, Spencer Clark, Leo Donner, and Lucas Harris for helpful discussions. N. J. is supported by a Harry Hess fellowship from the Princeton Department of Geosciences. We thank Leo Donner, Levi Silvers, and the two anonymous reviewers for constructive reviews.

References

Andrews, T., & Forster, P. M. (2010). The transient response of global-mean precipitation to increasing carbon dioxide levels. *Environmental Research Letters*, *5*(2), 25212.

Andrews, T., Forster, P. M., Boucher, O., Bellouin, N., & Jones, A. (2010). Precipitation, radiative forcing and global temperature change. *Geophysical Research Letters*, *37*, L14701. https://doi.org/10.1029/2010GL043991

Bala, G., Caldeira, K., & Nemani, R. (2010). Fast versus slow response in climate change: Implications for the global hydrological cycle. *Climate Dynamics*, *35*(2-3), 423–434.

Ball, F. (1960). Control of inversion height by surface heating. *Quarterly Journal of the Royal Meteorological Society*, *86*(370), 483–494.

Betts, A. (1973). Non-precipitating cumulus convection and its parameterization. *Quarterly Journal of the Royal Meteorological Society*, *419*, 178–196.

Betts, A. K. (2000). Idealized model for equilibrium boundary layer over land. *Journal of Hydrometeorology*, *6*, 507–523.

Betts, A. K., & Ridgway, W. (1989). Climatic equilibrium of the atmospheric convective boundary layer over a tropical ocean. *Journal of the Atmospheric Sciences*, *46*(17), 2621–2641.

Chen, S. H., & Sun, W. Y. (2002). A one-dimensional time dependent cloud model. *Journal of the Meteorological Society of Japan*, *80*(1), 99–118.

Cronin, T. W. (2013). A sensitivity theory for the equilibrium boundary layer over land. *Journal of Advances in Modeling Earth Systems*, *5*, 764–784. https://doi.org/10.1002/jame.20048

Dinh, T., & Fueglistaler, S. (2017). Mechanism of fast atmospheric energetic equilibration following radiative forcing by CO_2. *Journal of Advances in Modeling Earth Systems*, *9*, 2468–2482. https://doi.org/10.1002/2017MS001116

Fan, J., Rosenfeld, D., Yang, Y., Zhao, C., Leung, L. R., & Li, Z. (2015). Substantial contribution of anthropogenic air pollution to catastrophic floods in Southwest China. *Geophysical Research Letters*, *42*, 6066–6075. https://doi.org/10.1002/2015GL064479

Fildier, B., Parishani, H., & Collins, W. (2017). Simultaneous characterization of mesoscale and convective-scale tropical rainfall extremes and their dynamical and thermodynamic modes of change. *Journal of Advances in Modeling Earth Systems*, *9*, 2103–2119. https://doi.org/10.1002/2017MS001033

Fläschner, D., Mauritsen, T., & Stevens, B. (2016). Understanding the intermodel spread in global-mean hydrological sensitivity. *Journal of Climate*, *29*, 801–817. https://doi.org/10.1175/JCLI-D-15-0351.1

Hodzic, A., & Duvel, J. P. (2018). Impact of biomass burning aerosols on the diurnal cycle of convective clouds and precipitation over a tropical island. *Journal of Geophysical Research: Atmospheres*, *123*, 1017–1036. https://doi.org/10.1002/2017JD027521

Hong, S. Y., Noh, Y., & Dudhia, J. (2006). A new vertical diffusion package with an explicit treatment of entrainment processes. *Monthly Weather Review*, *134*(9), 2318–2341.

Kopparla, P., Fischer, E. M., Hannay, C., & Knutti, R. (2013). Improved simulation of extreme precipitation in a high-resolution atmosphere model. *Geophysical Research Letters*, *40*, 5803–5808. https://doi.org/10.1002/2013GL057866

Lee, S. S., Guo, J., & Li, Z. (2016). Delaying precipitation by air pollution over the Pearl River Delta: 2. Model simulations. *Journal of Geophysical Research: Atmospheres*, *121*, 11,739–11,760. https://doi.org/10.1002/2015JD024362

Lilly, D. K. (1968). Models of cloud-topped mixed layers under a strong inversion. *Quarterly Journal of the Royal Meteorological Society*, *94*(401), 292–309.

Lin, Y. L., Farley, R. D., & Orville, H. D. (1983). Bulk parameterization of the snow field in a cloud model. *Journal of Climate and Applied Meteorology*, *22*(6), 1065–1092.

Lutsko, N. J., & Cronin, T. W. (2018). Increase in precipitation efficiency with surface warming in radiative-convective equilibrium. *Journal of Advances in Modeling Earth Systems*, *10*, 2992–3010. https://doi.org/10.1029/2018MS001482

Ming, Y., Ramaswamy, V., & Persad, G. (2010). Two opposing effects of absorbing aerosols on global-mean precipitation. *Geophysical Research Letters*, *37*, L13701. https://doi.org/10.1029/2010GL042895

Muller, C. J., O'Gorman, P. A., & Back, L. E. (2011). Intensification of precipitation extremes with warming in a cloud-resolving model. *Journal of Climate*, *24*(11), 2784–2800.

Myhre, G., Shindell, D., Bréon, F. M., Collins, W., Fuglestvedt, J., Huang, J., & Zhang, H. (2013). Anthropogenic and natural radiative forcing. In T. Stocker (Ed.), *Climate Change 2013: The physical science basis. Contribution of Working Group I to the Fifth Assessment Report of the Intergovernmental Panel on Climate Change* (pp. 659–740). Cambridge, United Kingdom and New York, NY, USA: Cambridge University Press. https://doi.org/10.1017/CBO9781107415324.018

O'Brien, T. A., Collins, W. D., Kashinath, K., Rübel, O., Byna, S., Gu, J., & Ullrich, P. A. (2016). Resolution dependence of precipitation statistical fidelity in hindcast simulations. *Journal of Advances in Modeling Earth Systems*, *8*, 976–990. https://doi.org/10.1002/2016MS000671

O'Gorman, P. A. (2015). Precipitation extremes under climate change. *Current Climate Change Reports*, *1*(2), 49–59.

O'Gorman, P. A., & Schneider, T. (2009). The physical basis for increases in precipitation extremes in simulations of 21st-century climate change. *Proceedings of the National Academy of Sciences*, *106*(35), 14,773–14,777.

Pauluis, O., & Garner, S. (2006). Sensitivity of radiative–convective equilibrium simulations to horizontal resolution. *Journal of the Atmospheric Sciences*, *63*(7), 1910–1923.

Pendergrass, A. G., & Gerber, E. P. (2016). The rain is askew: Two idealized models relating vertical velocity and precipitation distributions in a warming world. *Journal of Climate*, *29*(18), 6445–6462.

Richardson, T. B., Forster, P. M., Andrews, T., & Parker, D. J. (2015). Understanding the rapid precipitation response to CO_2 and aerosol forcing on a regional scale. *Journal of Climate*, *29*, 583–594.

Romps, D. M. (2011). Response of tropical precipitation to global warming. *Journal of the Atmospheric Sciences*, *68*(1), 123–138.

Romps, D. M. (2017). Exact expression for the lifting condensation level. *Journal of the Atmospheric Sciences*, *74*(12), 3891–3900.

Rutledge, S. A., & Hobbs, P. V. (1984). The mesoscale and microscale structure and organization of clouds and precipitation in midlatitude cyclones. XII: A diagnostic modeling study of precipitation development in narrow cold-frontal rainbands. *Journal of the Atmospheric Sciences*, *41*(20), 2949–2972.

Sillmann, J., Kharin, V., Zhang, X., Zwiers, F., & Bronaugh, D. (2013). Climate extremes indices in the CMIP5 multimodel ensemble: Part 1. Model evaluation in the present climate. *Journal of Geophysical Research: Atmospheres*, *118*, 1716–1733. https://doi.org/10.1002/jgrd.50203

Sillmann, J., Stjern, C. W., Myhre, G., & Forster, P. M. (2017). Slow and fast responses of mean and extreme precipitation to different forcing in CMIP5 simulations. *Geophysical Research Letters*, *44*, 6383–6390. https://doi.org/10.1002/2017GL073229

Stephens, G. L., L'Ecuyer, T., Forbes, R., Gettelmen, A., Golaz, J. C., Bodas-Salcedo, A., & Haynes, J. (2010). Dreary state of precipitation in global models. *Journal of Geophysical Research*, *115*, D24211. https://doi.org/10.1029/2010JD014532

Strong, J. D., Vecchi, G. A., & Ginoux, P. (2015). The response of the tropical Atlantic and West African climate to Saharan dust in a fully coupled GCM. *Journal of Climate*, *28*(18), 7071–7092.

Takahashi, K. (2009). Radiative constraints on the hydrological cycle in an idealized radiative–convective equilibrium model. *Journal of the Atmospheric Sciences*, *66*(1), 77–91.

Tennekes, H. (1973). A model for the dynamics of the inversion above a convective boundary layer. *Journal of the Atmospheric Sciences*, *30*(4), 558–567.

Tompkins, A. M., & Semie, A. G. (2017). Organization of tropical convection in low vertical wind shears: Role of updraft entrainment. *Journal of Advances in Modeling Earth Systems*, *9*, 1046–1068. https://doi.org/10.1002/2016MS000802

Wang, S., & Sobel, A. H. (2011). Response of convection to relative sea surface temperature: Cloud-resolving simulations in two and three dimensions. *Journal of Geophysical Research*, *116*, D11119. https://doi.org/10.1029/2010JD015347

Wilcox, E. M., & Donner, L. J. (2007). The frequency of extreme rain events in satellite rain-rate estimates and an atmospheric general circulation model. *Journal of Climate*, *1*, 53–69.

Wing, A. A., & Cronin, T. W. (2016). Self-aggregation of convection in long channel geometry. *Quarterly Journal of the Royal Meteorological Society*, *142*(694), 1–15.

Zhao, M. (2014). An investigation of the connections among convection, clouds, and climate sensitivity in a global climate model. *Journal of Climate*, *27*(5), 1845–1862.